Ultrasound-guided Characterization of Interstitial Ablated Tissue Using RF Time Series: Feasibility Study

Farhad Imani, Purang Abolmaesumi, Mark Z. Wu, Andras Lasso, Everett C. Burdette, Goutam Ghoshal, Tamas Heffter, Emery Williams, Paul Neubauer, Gabor Fichtinger, and Parvin Mousavi

***Abstract*—This paper presents the results of a feasibility study to demonstrate the application of ultrasound RF time series imaging to accurately differentiate ablated and non-ablated tissue. *Methods:* For 12 *ex vivo* and two *in situ* tissue samples, RF ultrasound signals are acquired prior to, and following, high intensity ultrasound ablation. Spatial and temporal features of these signals are used to characterize ablated and non-ablated tissue in a supervised-learning framework. *Results:* In cross-validation evaluation, a subset of four features extracted from RF time series produce a classification accuracy of 84.5%, and an area under ROC curve of 0.91 for *ex vivo* data, and an accuracy of 85% for *in situ* data. *Conclusion:* Ultrasound RF time series is a promising approach for characterizing ablated tissue.**

***Index Terms*—tissue ablation, ultrasound RF time series, characterization of ablated tissue region.**

I. Introduction

Ablation therapy is an active field of study as a minimally invasive cancer treatment modality in the last few decades [1]. Using this modality, the surrounding tissue can be preserved while targeting specific tumour locations. Chemical, cryo, and thermal ablation are the techniques developed to achieve permanent destruction of tumours. Chemicals, chemotheraputic drugs, or radioactive isotopes are used as intralesionally-injected agents for attacking cancerous cells in the tissue. Yet, they result in incomplete necrosis of ablated lesions [2]. Cryoablation is another promising technique that causes tissue death by alternating cooling and thawing cycles, but was previously limited by the large size of cryoablators [3], [4]. With the development of ultrathin cryoprobes, it is currently possible to successfully target tumours less than three centimetres in diameter [5]. In thermal ablation, the target tissue is coagulated by transferring heat to the target area. There are many heat delivery mechanisms currently in use. Microwave energy directed at the tumour causes coagulation near the probe due to vibration of water molecules in the tissue [6], and has been used to treat tumours of various sizes [7]. Microwave ablation is not affected by the heat sink of large blood vessels located near the tumors as significantly as other thermal ablation techniques. The heat sink effect happens when the heat generated by the ablator is drawn away by flowing blood in the vessels. Although microwave ablation requires less ablation time, it is difficult to minimize the probe diameter which currently spans a few centimetres [8]. Laser therapy delivers heat in the form of high intensity light through small fibers and has been applied to irresectable hepatic tumours [9]. Laser photocoagulation can be performed in many clinical applications to target small tissue spots with high resolution. This method can be effective in up to $10\ mm$ depth of tissue [8]. In addition to its low penetration in depth, this approach is quite expensive and usually multiple sessions are required for therapy [10]. Particularly popular is radio frequency ablation, in which an electrode is inserted into a grounded patient and radio frequency current coagulates the target tissue [11]. This procedure has two major drawbacks: inadvertent charring of tissue creates thermal insulation, and the presence of nearby heat sinks (e.g. blood vessels) can draw heat away from the desired target [12].

High Intensity Focused Ultrasound (HIFU) is an approach to thermal ablation that has been utilized for cancer treatment since the 1940s [1]. In this approach, high levels of acoustic energy are deposited into the tissue at the localized focus of an ultrasound transducer for a short duration. This causes rapid temperature elevation and coagulation necrosis in the tissue. HIFU is considered a minimally invasive tissue ablation method that can be used to ablate tumors deep in the body [13]. More recent advances include the development of interventional devices that emit directional and conformable high intensity ultrasound delivered via a needle or catheter to achieve sensitive controlling of heating patterns [14]. These devices are termed ultrasound interstitial thermal therapy applicators (USITT), and are used in the study presented in the current paper [15].

The limitation associated with ablation therapy is primarily the difficulties in monitoring the temperature rise and the extent of the ablated region in the tissue. Some devices make use of built-in thermistors that are in close proximity to the ablation probe to crudely monitor the extent of ablation based on temperature readings [16]. Several image-based approaches with MRI and ultrasound have been proposed to address this issue. MRI can provide non-invasive thermometry with an excellent contrast in soft tissue by measuring the frequency

F. Imani is with the Electrical and Computer Engineering Department of Queen's university, Kingston, ON, Canada (farhad@cs.queensu.ca).

P. Abolmaesumi is with the Department of Electrical and Computer Engineering, University of British Columbia, Vancouver, BC, Canada.

E. C. Burdette, G. Ghoshal, T. Heffter, E. Williams and P. Neubauer are with Acoustic MedSystems Incorporation, IL, USA.

M.Z. Wu, A. Lasso, G. Fichtinger, and P. Mousavi are with the School of Computing, Queens University, Kingston, ON, Canada.

of MR signal (i.e. proton resonance frequency) [17]. Highly promising results have been reported using MRI thermometry, with a primary focus on prostate ablation therapy [18]. The main drawbacks of using MRI in visualizing thermal therapy are its high cost and low temporal resolution [19].

Ultrasound-based techniques for evaluating heat-induced lesions following thermal ablation have also been used by several groups. B-mode ultrasound imaging is one method for analysis of the ablated regions in the tissue [20], [21]. In this modality, changes in echogenicity enable the visualization of ablated regions. The negative side of an acoustic pressure wave may generate gas or vapour filled cavities in the tissue. This cavitation is usually the main reason for hyperechoic occurrence; however, the phenomenon is unpredictable and not a reliable factor to identify ablated regions [22], [23]. Several methods are also developed to estimate the temperature increase during the ablation process by detecting the change of sound speed, attenuation coefficient, and backscattering [23] [24], [25], [26]. By increasing the temperature in the tissue, the speed of sound generally increases (except in fatty tissue) which causes a time shift in ultrasound Radio-Frequency (RF) echoes, referred to as virtual shift [26]. Studies have shown major limitations of using speed of sound for detecting ablated lesions. Such limitations include the nonlinear relationship between speed of sound and temperature [25] and its variability with the proportion of fat in the tissue [23]. It has also been reported that there is an increase in the integrated backscatter and attenuation coefficient in the region of ablation for various *ex vivo* animal experiments [24], [27], [28]. Spectral analysis of ultrasound RF signals in a single RF frame, which is related to the physical scatterer properties, is used in the literature to characterize coagulated tissue for *ex vivo* and *in vivo* experiments at high and clinical ultrasound frequencies [20], [29], [30]. Ultrasound elastography has emerged as another technique to augment conventional ultrasound imaging for monitoring the ablation zone [16]. Following a tissue displacement generated by an external mechanical stimulus or using high energy acoustic radiation, various elastic properties of the tissue are calculated from ultrasound images to identify stiffer ablated regions [31], [32]. Although the computed strain images have been reported to be in good agreement with gross pathology, this approach either requires additional hardware for external excitation of the tissue, or a modification to the diagnostic ultrasound image sequence to apply high energy acoustic radiation forces.

Recently, our group has proposed a tissue typing approach that uses a time series of ultrasound RF frames acquired from a fixed location in the tissue. This method has been effectively applied for tissue classification at both high and clinical frequencies [33]. We have also improved the tissue classification results achieved using this method by applying wavelet transform [34], and depth-dependent phase shift of RF time series [35]. The feasibility of this method for ablation region classification was demonstrated in a limited study with three tissue samples [36]. We showed that the RF time series features were consistent within each tissue sample; however, no attempt was made to predict the ablation region in a tissue based on the features obtained in other tissue samples.

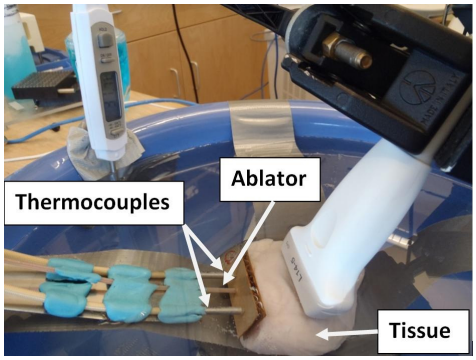

Fig. 1. Tissue ablation and data acquisition setup. Three prongs enter the tissue from the left: the ablator in the middle, and thermocouples at distances of 7.5 and 15 mm.

In this paper, we demonstrate the potential of RF time series to classify ablated and non-ablated regions of tissue in ultrasound images, following tissue coagulation, through a set of controlled laboratory experiments. We show that the characterization of ablated regions in a set of tissue samples can be effectively extrapolated to classify the ablated regions in a never-before-seen tissue sample. We achieve this by training a classifier based on features extracted from the tissue samples, and distinguishing between ablated and non-ablated regions of tissue through a leave-one-out tissue sample cross-validation. A detailed validation is presented using ultrasound RF data acquired from 12 *ex vivo* tissue samples following USITT ablation. We demonstrate the capability of the RF time series features to classify ablated regions of never-before-seen tissue samples along with their consistency and superiority over the spectral features of a single RF frame previously reported in the literature [20], [29], [30], [38]. Finally, we perform a feasibility study for classification of ablated tissue in *in situ* bovine liver using RF time series features.

II. Materials and Methods

A. Data Acquisition

A USITT applicator (Acoustic MedSystems, Champaign, IL) [14], [15] is used for coagulation of 12 homogeneous chicken breast tissue specimens purchased from the grocery store. For each experiment, the tissue sample is submerged in water heated to $37°C$. Water from a temperature-controlled reservoir is pumped into a stainless steel heat exchanger under the tissue to maintain the temperature of the water bath. Two type T thermocouples (Physitemp Instruments, Clifton, NJ) mounted parallel to the applicator, are inserted with the needle-based ablation applicator in the tissue (Fig. 1). One thermocouple is positioned at 7.5 mm and another thermocouple at 15 mm from the applicator. Each thermocouple contains three thermal sensors located at the tip, and 0.5 cm, and 1 cm from the tip. Degassed water is pumped through the inside of the hollow applicator and out over the surface of the transducers at a rate of 25 ml/min. Water cooling is crucial for the applicator, as it removes heat from the piezoelectric elements and allows the transducer to be operated at higher power levels. The ablator is configured to transmit non-focused

acoustic energy in the form of longitudinal pressure waves of 10 Watts, using two cylindrical piezoelectric transducers. The spatial peak temporal average intensity (I) is calculated as:

$$I = Sound\ Power/(4\pi r^2), \tag{1}$$

where $Sound\ Power$ for the transducer is approximately 50% of the input power (50% of 10 Watts), and r is the distance from the transducer. Ablation-induced heating increases the thermal dose to the tissue, until at least one sensor on the thermocouples consistently displays a reading above $45°C$ and the equivalent minute dose (t_{43}) corresponding to the location of that sensor reaches 250 [14], [39]. Ablation is then terminated and the tissue is allowed to cool down for eight minutes.

An Ultrasonix SonixTouch scanner (Ultrasonix, Richmond, BC) with a L14-5/38 linear array transducer (Ultrasonix, Richmond, BC) is used to collect ultrasound RF time series signals prior to, and at the end of the ablation process. The ultrasound probe, thermocouples and the ablator are fixed using two mechanical arms during the ablation process, and the chicken tissue is placed on duct tape immersed in water. Substantial care is taken to avoid any macroscopic motion while tissue coagulation progresses. Data is acquired from the tissue along the transducer plane and perpendicular to the ablator and thermocouples (i.e. the same plane as the tissue is sliced at the end of the ablation). The central frequency of the probe is 6.6 MHz, and the focal point is set to 1–2 cm, i.e. approximately the same imaging depth as the tip of the ablator. The power is set the maximum clinical value available for the machine, and the scanner is configured to acquire 128 frames, at the rate of 45 frames/sec (22.22 ms temporal resolution). Each RF frame contains 256 scan lines laterally and 1168 samples axially that correspond to 38 mm $\times$ 45 mm spatially. The RF signals acquired from the tissue are sampled using an A/D with a sampling rate of 20 MHz.

B. Registration and Region of Interest Selection

The ablated regions of the tissue are verified using the corresponding gross pathology images. Following ablation, each tissue sample is cut approximately along the data acquisition plane. The corresponding plane of the tissue is shown in Fig. 2 on the left hand side. This plane is found by guiding the cut with two lines, marked on the tissue surface, approximating the axis and tilt of the ultrasound probe on the tissue. Landmarks for registration are the tip of ablator, and two thermocouples marked by the black circle and X, respectively in Fig. 2. The location of the ablator and thermocouples are readily discerned in ultrasound as they appear bright white and cast prominent hypoechoic shadows. In the case of the tissue, the ablator leaves a gaping hole once it is removed that is immediately visible, but locating where the thermocouples intersect with the plane of interest is more complex as it is common to see small, natural perforations in the tissue of a similar diameter. However, the distinct shape of the recess created by the thermocouple and the fact that it is a known distance from the ablator allows the match to be made in the tissue. With these landmarks localized in both ultrasound and tissue, it is then possible to select ablated and non-ablated regions of interest (ROIs).

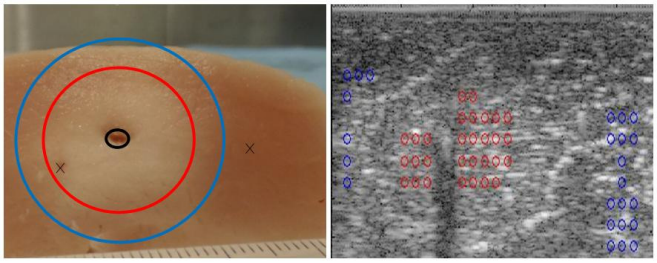

Fig. 2. Left: Matching slice of the tissue with the ablation zone delineated. The black circle and "x" indicate ablator and thermocouples, respectively. Right: ROI selection from B-mode images; ablated and non-ablated ROIs are picked from the areas inside the red circle, and outside the blue circle, respectively. The area between these circles is not used for ROI selection.

Sixty equally-sized ROIs from ablated and non-ablated regions of the tissue are selected in each tissue sample, resulting in a total of 720 ROIs. Each ROI is the time series data from a 2.08 mm (axially) $\times$ 1.21 mm (laterally) section of an image frame, while the distances between each two samples in axial and lateral directions are 0.0385 mm and 0.1484 mm, respectively. In other words, an ROI is a three dimensional signal with 54 axial, 8 lateral and 128 time samples. The wavelength of ultrasound for the transducer central frequency of 6.6 MHz is 0.23 mm, assuming the speed of sound in soft tissue to be 1540 m/s. The axial sample size allows for having a reasonable number of ROIs in that direction (20 ROIs). The ratio of the number of selected ablated to non-ablated ROIs is approximately 1:1. Any mis-registration errors have been handled by only selecting ROIs that were very close to the ablator tip or safely far from it. As depicted in Fig. 2, for each tissue sample cut, the selected ablated ROIs are located less than 0.8 cm from the tip of the ablator (inside the red circle), whereas the non-ablated ROIs are at a distance of 1.2 cm or greater from the tip of the ablator tip (outside the blue circle). Therefore, we have avoided using the ROIs located close to the approximate boundary of the ablated regions, i.e. the area between blue and red circles.

C. Feature Extraction

Tissue characterization of ablated and non-ablated ROIs of each tissue specimen is performed by extracting the features of the acquired ultrasound RF time series data. Each ultrasound RF time series is a discrete signal containing N sequentially acquired frames from each sample of the imaging plane. The ultrasound RF time series of sample l, as a function of acquired frames n is as below:

$$x_l(n); \quad n = 1, ..., N, \tag{2}$$

where $N = 128$ is the length of the time series or acquired frames. Since we are interested in the variation of the signal, its mean is subtracted:

$$\hat{x_l}(n) = x_l(n) - \bar{x}, \quad and \quad \bar{x} = \frac{1}{N}\sum_{l=1}^{N} x_l(n). \tag{3}$$

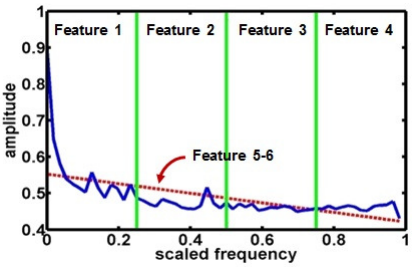

Fig. 3. The spectral features of RF time series where the vertical bars delineate the four frequency bands. The red-dotted line represents a line of best-fit.

TABLE I
A SUMMARY OF THE RF TIME SERIES FEATURES PROPOSED IN THIS PAPER AND THE SPECTRAL FEATURES OF A SINGLE RF FRAME USED FOR ABLATED TISSUE CLASSIFICATION.

RF time series features	
Feature	Description
1-4	The sums of the amplitude spectrum in the four quarters of the frequency range.
5-6	Intercept and slope of the line fitted to the entire spectrum.
7	Fractal dimension of the RF time series.
8-9	Intercept and slope of the line fitted to the Central Frequency (CF) values as a function of depth for each ROI.
10	Mean Central Frequency (MCF) in an ROI.
Spectral features in a single RF frame	
Feature	Description
11-12	Intercept and slope of the regression line to RF signal in spectral domain.
13	Average of the power spectrum of the RF signal over the bandwidth.

A discrete Fourier transform is applied on the zero-mean RF time series of sample l as below:

$$X_l(k) = \frac{1}{N}\sum_{l=1}^{N} \hat{x_l}(n) e^{-j2\Pi kn/N} \tag{4}$$

The corresponding power spectrum of sample l for $X_l(k)$ is then computed. The power spectrum is calculated for all samples in an ROI (54×8 samples), and averaged. As such, each ROI is represented by a single "averaged" power spectrum of length N. The average spectrum is then normalized through dividing it by its maximum.

Ten features, previously reported by our group for tissue characterization, are extracted from the RF time series signal and summarized in Table I [33], [35], [36], [37]. Features include the sums of the power spectrum in four frequency bands (Features 1-4) depicted in Fig. 3, calculated as:

$$Feature(i) = \sum_{k=1+(i-1)N/8}^{Ni/8} |X_{ROI}(k)|, i = 1...4. \tag{5}$$

The frequency range of the power spectrum is between 0–22.5 Hz (45 frames/second). Due to symmetry, only the positive frequency components ($X_{ROI}(i)$, $i = 1...N/2$) have been used to reduce the computational complexity. The slope and intercept of the best-fit line to the entire power spectrum, and fractal dimension constitute features 5–7.

Fractal dimension is calculated using Higuchi's method for all samples in an ROI (54×8 samples) and averaged over each ROI. Implementation details of Higuchi's method are offered elsewhere [33], [37], [40].

Central Frequency as a function of depth (CF(z)) is defined for each spatial sample in the RF data as the mean of bandwidth of the power spectrum of its corresponding time series [35]:

$$CF(z) = \frac{\sum_{i=1}^{N/2} f_i.PSD(f_i)}{\sum_{i=1}^{N/2} PSD(f_i)}, \tag{6}$$

where $PSD(f)$ is the power spectrum density of RF time series, and z is the distance from the transducer in depth (axial direction). For each axial distance (54 points in total) in an ROI, CF values are averaged over the eight lateral samples. A regression line is then fitted to the data distribution of the resulting 54 points. The slope, and the intercept of this line consitute features 8 and 9. The mean of all CF values in an ROI constitutes feature 10 and is called Mean Central Frequency (MCF).

D. Classification

A Support Vector Machine (SVM) classifier is used to classify ablated and non-ablated ROIs[1]. This classifier finds an optimal hyperplane with maximum margin separating the data into two classes (usually in a higher dimensional space). Specifically, given a set of real-valued training vectors x_i, $i = 1, ..., n$ and corresponding labels $y_i \in (1, -1)$, the goal is to find W, b, and ξ_i that minimizes the following cost function:

$$\frac{1}{2}W^T W + C\sum_{i=1}^{n} \xi_i, \tag{7}$$

subject to

$$y_i(W^T\phi(x_i) + b) \geq 1 - \xi_i,\ \xi_i \geq 0,\ \ for\ \ i = 1, ..., n. \tag{8}$$

The ξ_i allows for misclassification of imperfect data, $C > 0$ is the penalty parameter that regulates the ξ_i, and ϕ is the function that maps the training data into a higher dimensional space. The kernel function defines dot products in this space: $K(x_a, x_b) = \phi(x_a)^T\phi(x_b)$. The radial basis function (RBF) is our kernel of choice due to its ease of initialization (possessing a single parameter, γ) and classification accuracy [33]:

$$RBF(x_a, x_b) = exp(-\gamma \left\|x_a - x_b\right\|^2),\ \ \gamma > 0. \tag{9}$$

We optimize the only parameter of the RBF kernel function, γ, and the penalty parameter C by an exhaustive search to achieve the highest classification accuracy. To find the best classifier parameters, we perform a coarse followed by a fine search to reduce the computational complexity. The SVM library we used provides class posterior probability estimates, in addition to class labels, for each data point.

[1]A Library for SVMs: http://www.csie.ntu.edu.tw/~cjlin/libsvm/

E. Feature Reduction and Cross-Validation

Clinically, the most relevant evaluation of our proposed approach for identifying ablated regions is to use a classifier trained with the best features from a selected group of tissue samples, and successfully classifying the ablation region in a never-before-seen tissue sample. We refer to this as *leave-one-out tissue sample* cross-validation. In this framework, we exhaustively search for the best subset of time series features (amongst the proposed 10 time series features) for classification of ablated and non-ablated tissue. We further evaluate the consistency of the time series features within each tissue sample and in pooled data from all tissue samples. The three cross-validation tests we perform are as follows:

Leave-one-out tissue sample evaluation: In this evaluation, the classifier is built using features from the ROIs of previous tissue samples, with known labels, and applied to ROIs of the current tissue sample. To characterize the ablated tissue, the best subset of RF time series features common to all leave-one-out tissue sample evaluations is selected. We exhaustively search for subsets of one to six time series features. We noticed that larger number of features resulted in reduced classification accuracies. The selected subset of the best features from RF time series is used in the next two evaluation tests.

Intra-tissue sample evaluation: To determine the consistency of the selected subset of RF time series features in individual tissue samples, we use these features to classify ablated and non-ablated ROIs in each tissue sample separately.

Pooled tissue sample evaluation: To further study the consistency of RF time series features across the larger context of all tissue samples, ROIs are pooled from all tissue samples and ablated regions are identified.

Leave-one-out tissue sample evaluation is a cross-validation experiment achieved by running the SVM classifier 12 times. Each run is performed by training on features extracted from 11 tissue samples and testing on the remaining 12th tissue sample. To implement the SVM classifier for intra-tissue sample and pooled tissue sample evaluations, a five-fold cross validation strategy is performed. ROIs are randomly divided in five parts; five classifiers are trained each using four different parts of the data, with the remaining part used for testing. In order to remove the effect of bias in data division, ROIs are reordered and the entire process is repeated 50 times. The average accuracies are reported over these 250 runs.

F. Effects of ROI Size and RF Time Series Length

We analyzed the effect of ROI size on the classification outcome. We performed experiments using three sizes: i) ROI size 1 (smaller size): $x/2 \times y/2$, ii) ROI size 2 (original size, used in this paper): $x \times y$, and iii) ROI size 3 (larger size): $2x \times 2y$, where $x = 1.21\ mm$ in the lateral direction and $y = 2.08\ mm$ in the axial direction. The smaller size ROIs are generated by dividing each original size ROI into 4 ROIs, and the larger ROIs are made by combining the adjacent ROIs.

In addition, for the *ex vivo* data, we chose three RF time series lengths (16, 64, and 128 frames) for tissue characterization. We calculated the classification accuracies using the best common subsets of RF time series features with these three lengths for all three cross-validation evaluation methodologies.

TABLE II
CLASSIFICATION ACCURACIES, AND THE AREA UNDER ROC CURVE FOR LEAVE-ONE-OUT TISSUE SAMPLE, INTRA-TISSUE SAMPLE, AND POOLED TISSUE SAMPLE EVALUATIONS USING THE BEST COMMON SUBSET OF RF TIME SERIES FEATURES.

	Average mean and STD of classification accuracies	Average area under ROC curve
Leave-one-out tissue sample	84.43±9.84%	0.91
Intra-tissue sample	89.48±8.79%	0.94
Pooled tissue sample	85.55±0.95%	0.91

G. Characterization of Ablation Using a Single RF Frame

We compare the performance of RF time series features with the spectral features of a single RF frame [20], [29], [30], [38]. To extract the spectral features of a single RF frame, each frame is passed through a Hamming window and calibrated to remove variations due to transducer and electrical components. Calibration approaches presented in the literature either use a planar reflector [37], [38], [41], or reference phantom techniques [30]. Here, we closely implement the calibration method proposed in [38], [41], [42], [43], [44]. A planar reflector in the form of a thick piece of glass immersed in water is used, and the gain of the receiver amplifier is adjusted to its minimum to avoid signal saturation due to large amplitude echoes. The power spectrum of the windowed RF data for each scan line ($S^i_{win}(z,f)$) is divided by the power spectrum of the RF data acquired from the surface of the glass ($S^i_{glass}(z,f)$) [37][38][41]:

$$S^i_{cal}(z,f) = \frac{S^i_{win}(z,f)}{S^i_{glass}(z,f)}, i = 1...8 \tag{10}$$

where i represents the scan lines in a window and z is the axial distance from the transducer. The resulting signal ($S^i_{cal}(z,f)$) is used to extract three spectral features as shown in Table I. The intercept and slope of the regression line fitted to the portion of the power spectrum that lies in the transducer frequency band (5–10 MHz), and the average spectrum in this band constitute features 11–13. The spectral features of a single RF frame are computed for every scan line of each ROI, and averaged over that ROI [37]. To compensate for the effect of attenuation, we correct the values of the slope and mean of the power spectrum of a single RF frame by applying an assumed linear attenuation coefficient of 0.5 dB/cm/MHz [38], [41].

III. RESULTS

A. Leave-One-Out Tissue Sample Evaluation

The verification of the proposed approach is performed by learning from a series of tissue samples in order to extend the method to future independent tissue samples. We determined that the feature subset with the best classification result is made up of features 2, 3, 5, and 10. The histograms of these four features across all 12 tissue samples, prior to and following ablation, are depicted in Fig. 4. The best classifier parameters using the RBF kernel function are $C = 12$ and $\gamma = 7$, computed from an exhaustive search. The classification results for 12 leave-one-out tissue sample evaluations are displayed by

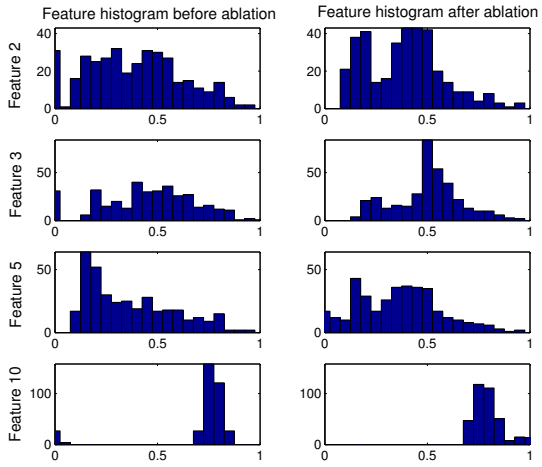

Fig. 4. Histograms of the selected RF time series features prior to and following ablation using the ultrasound data acquired from 12 tissue samples. Each feature is normalized between the minimum and maximum values of that feature across all values obtained prior to and following ablation.

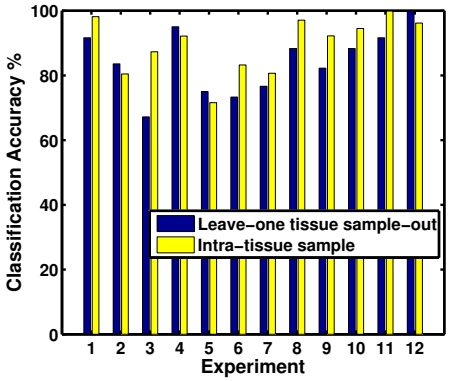

Fig. 5. Classification accuracies for 12 leave-one-out tissue sample and intra-tissue sample evaluations using the best common subset of RF time series features.

blue bars in Fig. 5. Each blue bar corresponds to the accuracy of identifying ablated and non-ablated ROIs when that tissue sample is left out for testing and features from all other tissue samples are used for training. The averages of these results are also presented in Table II. The classification accuracy achieved using the best subset of RF time series features for 12 tissue samples varies between 67% and 100% with an average of 84.43%. The Receiver Operating Characteristic (ROC) curve for leave-one-out tissue sample evaluation is also shown in Fig. 6 as the blue-solid line. The average area under the ROC curve using the best RF time series features is 0.91, as presented in Table II.

Applying the RF time series features to classify the entire imaging plane (and not just the ROIs used for testing the classification accuracy) results in the colormaps shown in Fig. 7. These colormaps are generated through leave-one-out tissue sample evaluation and using the class posterior probability estimates provided by the SVM classifier. In Fig. 7, tissue ablation is predicted for the entire imaging planes

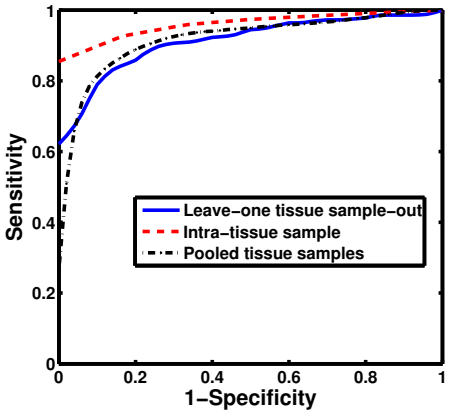

Fig. 6. ROC curves for leave-one-out tissue sample, intra-tissue sample, and pooled tissue sample evaluations using the best common subset of RF time series features.

for three tissue samples at the end of the cooling period (bottom right images in (a), (b) and (c)). Corresponding gross pathology for each tissue sample is also shown to compare the predicted zone of ablation (bottom left images in (a), (b) and (c)). As seen, the areas of ablation are not readily visible in B-mode images. Although the colormaps are generated for the entire B-mode image, we only display those ROIs that have a 0.3 or greater probability of being ablated.

B. Intra-Tissue Sample Evaluation

The consistency of the selected subset of RF time series features is examined to classify the ablated regions of each tissue sample individually. The features used are those identified as the best RF time series features from leave-one-out tissue sample evaluations. The optimal classifier parameters (C and γ) were determined from the leave-one-out tissue sample evaluations as well (as described in Section III.A), and the same parameters were used for all tissue samples in the intra-tissue sample evaluations. In each intra-tissue evaluation, 30 ablated and 30 non-ablated ROIs were selected where 80% were used for training and 20% were used for testing the classification results. The classification accuracies for each of the 12 tissue samples are computed independently as shown by yellow bars in Fig. 5 and then averaged as presented in Table II. Each yellow bar corresponds to the accuracy of identifying ablated and non-ablated ROIs when 20% of the ROIs in each tissue sample are selected randomly for testing and features from the remaining ROIs are used for training. The process of data division and reordering the ROIs is repeated 250 times and the average accuracies are presented using the selected subset of features and optimal classifier parameters. The classification accuracies using the best subset of RF time series features over all tissue samples vary between 72-100% with an average of 89.48%. Moreover, the ROC curve for intra-tissue sample evaluation is plotted in Fig. 6 as a red dashed line. The average area under this ROC curve using RF time series is 0.94 (Table II).

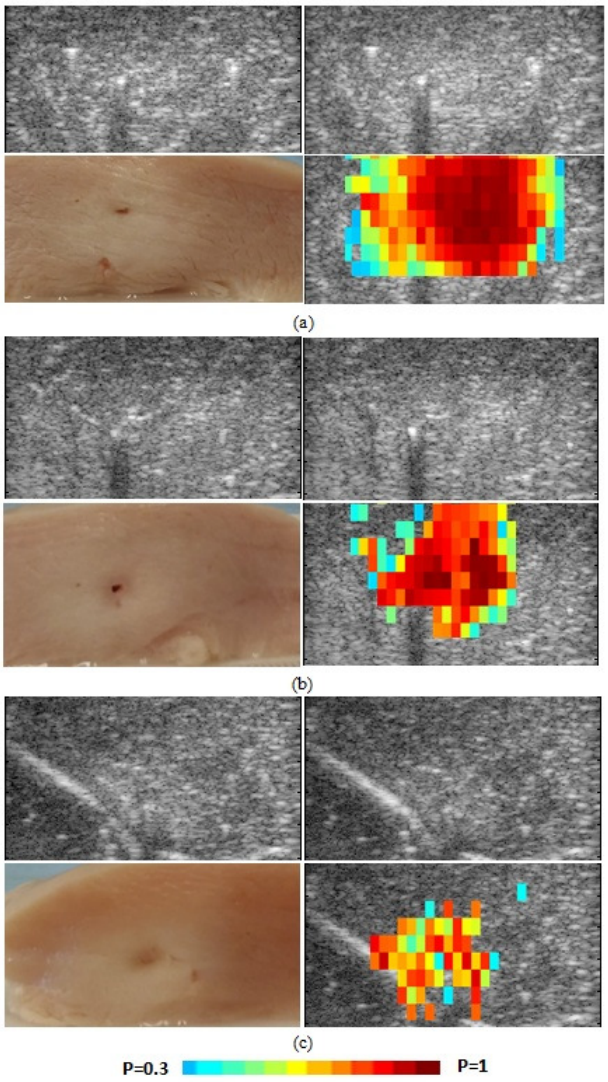

Fig. 7. B-mode images prior to (top left), and following ablation (top right), colormaps of posterior probabilities of ablated regions (bottom right), and their corresponding gross pathology images (bottom left) for three tissue samples (a, b, and c). Colormaps are generated by using four RF time series features extracted from a limited number of ROIs for each tissue, and extending the ablated tissue classification results to the entire image using the leave-one-out tissue sample evaluation. Only the ROIs that have a 0.3 or greater probability of being ablated are displayed. Note that the ablation zone is not visible in the B-mode images after the ablation.

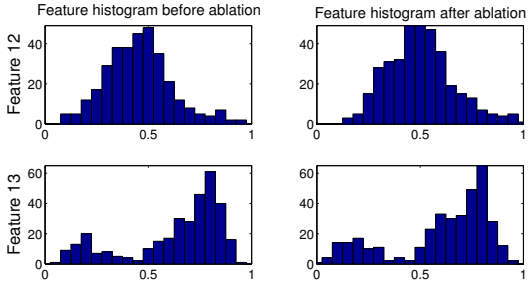

Fig. 8. Histograms of the selected spectral features of a single RF frame prior to and following ablation using the ultrasound data acquired from all tissue samples. Each feature is normalized between the minimum and maximum values of that feature across all values obtained prior to and after ablation.

TABLE III
CLASSIFICATION ACCURACIES USING THREE ROI SIZES USING THE BEST COMMON SUBSETS OF RF TIME SERIES FEATURES.

	ROI size 1	ROI size 2	ROI size 3
Leave-one-out tissue sample	80.29±12.95%	84.43±9.84%	80.62±13.81%
Intra-tissue sample	90.62±8.67%	89.48±8.79%	77.58±18.38%
Pooled tissue sample	86.33±0.93%	85.55±0.95%	72.57±1.95%

TABLE IV
CLASSIFICATION ACCURACIES USING THREE RF TIME SERIES LENGTHS USING THE BEST COMMON SUBSETS OF RF TIME SERIES FEATURES.

Time series length	128	64	16
Leave-one-out tissue sample	84.43±9.84%	78.77±8.02%	59.19±16.74%
Intra-tissue sample	89.48±8.79%	89.20±8.37%	89.67±12.14%
Pooled tissue sample	85.55±0.95%	86.76±0.52%	79.69±0.7%

C. Pooled Tissue Sample Evaluation

While cross-validation accuracy achieved using RF time series features is high within an individual tissue sample, it only demonstrates the consistency of ablated and non-ablated tissue and its corresponding features in that tissue sample. It is important to determine the classification performance in the larger context of all available data. Table II shows the results of pooling data from the 12 tissue samples into one large cross-validation test. The classification accuracy shown in this table (85.55±0.95%) is achieved using the best subset of RF time series features as determined in the leave-one-out tissue sample evaluation, and the same optimal classification parameters as in previous sub-sections. Moreover, the ROC curves generated using the best subsets of RF time series is plotted in Fig. 6 as black dash-dotted. The area under the ROC curve is 0.91 as presented in Table II.

D. Effects of ROI Size and RF Time Series Length

Effect of ROI size: The cross-validation accuracies achieved for three strategies using the best selected RF time series features are listed in Table III. From this table, it is clear that original size ROIs (size-2 ROIs), result in the highest classification accuracies for leave-one-out tissue sample cross validation. In addition the results using this size of ROIs are more consistent for all three cross-validation evaluations compared to other sizes of ROIs.

Effect of RF time series length: The classification accuracies using the best common subsets of RF time series features with three lengths of time series are presented in Table IV for leave-one-out tissue sample, intra-tissue sample, and pooled tissue sample evaluations. We show that by reducing the time series length from 128 to 64 samples, classification accuracy for leave-one-out tissue sample evaluation decreases slightly, while intra-tissue sample and pooled tissue sample evaluation results do not change significantly. However, a substantial change in the length of the RF time series (to 16 frames of the RF signal) reduces the classification results substantially.

TABLE V
CLASSIFICATION ACCURACIES, AND THE AREA UNDER THE ROC CURVE USING THE BEST COMMON SUBSET OF SPECTRAL FEATURES OF A SINGLE RF FRAME.

	Average mean and STD of classification accuracies	Average area under ROC curve
Leave-one-out tissue sample	55.73±10.27%	0.60
Intra-tissue sample	57.13±11.25%	0.63
Pooled tissue sample	55.03±1.35%	0.58

E. Characterization of Ablation Using a Single RF Frame

We compare the performance of the identified RF time series feature set with the best subset of spectral features of a single RF frame for classifying ablated regions. The best subset of spectral features from a single RF frame common to all leave-one-out tissue sample evaluations are spectral features 12 and 13, computed from an exhaustive search. The histograms for these two features across all 12 tissue samples, prior to and following ablation, are shown in Fig. 8. The classification accuracies for 12 leave-one-out tissue sample evaluations vary from 44% to 73% with an average of 55.73% for the best spectral features of a single RF frame as presented in Table V. The results achieved by the RF time series for leave-one-out tissue sample evaluation show statistically significant improvements over the classification results obtained by the spectrum of a single RF frame ($p = 10^{-9}$) using a two-tailed t-test analysis with 95% confidence interval. Furthermore, the classification results for 12 intra-tissue sample evaluations are in the range of 33-68% with an average of 57.13% for the best spectral features of a single RF frame. When performing the classifier on a larger context of data in pooled tissue sample evaluation, the classification accuracy achieved using the best spectral features of a single RF frame is 55.03±1.35%.

IV. DISCUSSION AND CONCLUSION

This paper presents characterization of ablated tissue regions, using RF ultrasound time series, in a detailed cross-validation and classification framework. An average classification accuracy of above 84%, and an area under ROC curve of 0.91 are achieved using a subset of only four RF time series features. These results are obtained by training a classifier on a selected group of tissue samples and extending its predictions to a never-before-seen tissue sample. The best subset of RF time series features are selected exhaustively from the 10 calculated features. This combination of RF time series features demonstrates the capability of the amplitude spectrum (features 2, 3, and 5), and the mean central frequency of the power spectrum density (feature 10) of the RF time series signal for characterization of ablated tissue regions across 12 leave-one-out tissue sample evaluations. From the histograms of these four features, and given the high classification accuracies, the combinatorial power of the features for tissue differentiation appears to be important. High classification accuracies and areas-under-ROC-curves for intra-tissue sample and pooled tissue sample evaluations demonstrate the consistency of RF time series features for each tissue sample individually, and in the larger context of all tissue samples.

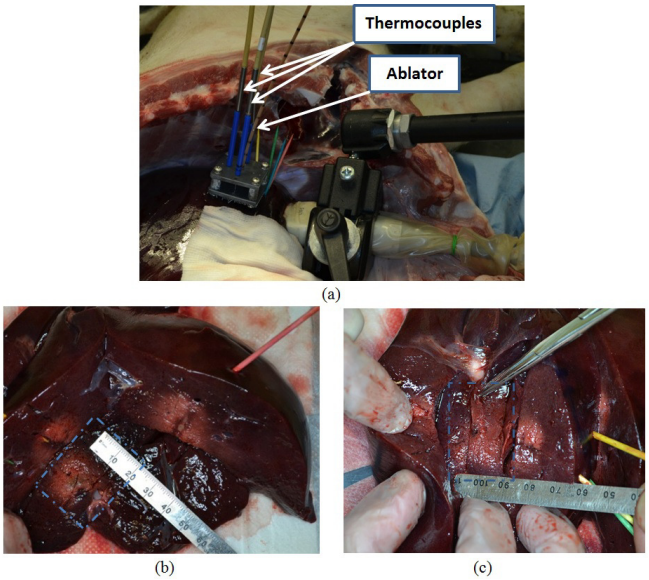

Fig. 9. (a) In situ liver ablation and data acquisition setup. Four prongs enter the tissue: the ablator in the middle, and thermocouples at distances of 1.5, 1, and 1 cm. (b and c) Ablated slices of the tissue corresponding to the ultrasound imaging planes. The planes of ultrasound images are shown as blue rectangles.

Tissue classification results also show that ablated tissue classification obtained by the RF time series features substantially outperforms that of the spectral features of a single RF frame. Adding spectral features of a single RF frame to the best subset of time series features did not improve the classification results. As the histograms of the spectral features of a single RF frame show, these features do not substantially change after ablation.

While our *ex vivo* evaluations are highly promising and demonstrate the potential of the RF time series approach for thermal ablation monitoring applications, the performance of the method is yet to be determined in *in vivo* conditions. Towards this goal, we carryout a feasibility *in situ* experiment.

In situ evaluation: We perform *in situ* ablation experiments on porcine liver in the operating room immediately after an animal is sacrificed. We ablat two spatially distinct locations of the liver in the animal using the USITT applicator (referred as two independent tissue samples in the remainder of this sub-section). As depicted in Fig. 9 (a), the ablator is inserted in the liver and three sets of thermocouples asre placed at 1.5 cm, and 1 cm on each side of the applicator. The placement of the thermal sensors is similar to our *ex vivo* experiments. Ultrasound imaging is performed using a mechanically fixed transducer in a plane perpendicular to ablation, similar to our previous experiments. The ablator is configured to transmit non-focused acoustic energy in the form of longitudinal pressure waves of 15 Watts, using two cylindrical piezoelectric transducers. Ablation-induced heating increases the thermal dose to the tissue, until at least the equivalent minute dose corresponding to the location of one sensor reaches 10^6.

The ablation regions for these experiments are shown in

Fig. 9 (b and c). We calculate the same four RF time series features that we used to classify the *ex vivo* tissue samples, from the ablated and non-ablated ROIs in the *in situ* data. The classification results for training and testing using ROIs picked from the same ablation location (equivalent to intra-tissue sample evaluation in the *ex vivo* experiment) are 96% and 98% within each ablation location. When training the classifier on features extracted from the ROIs of one ablation location and testing on the ROIs of the other ablation location (equivalent to leave-one-out tissue sample evaluation in the *ex vivo* experiments), the classification accuracies are 77% and 93% (an average of 85%). Using the feature reduction approach described in Section II.E, we exhaustively search for the feature subset that leads to the best leave-one-out tissue sample classification results for *in situ* experiments. We determine that a combination of features 1 and 2 (i.e., the sum of the absolute spectrum in the first and second quarters) provide the highest classification rate of 85% and 100% in the two tissue locations. From our experiments, it appears that the best feature subset for classification is tissue specific and is different between the *ex vivo* chicken breast study, and the *in situ* porcine liver study.

Although these experiments more closely mimic *in vivo* conditions, two factors are still not taken into account: in-plane and out-of-plane motion due to respiration, perfusion or other reasons. To minimize the effect of in-plane motion, deformable intra-frame registration could be used [45]. Reducing the ultrasound acquisition time while monitoring breathing, could also potentially mitigate the respiration-induced motion. Ultrasound acquisition time can be reduced by increasing the frame rate, or decreasing the total number of acquired frames. The specific frame rate required to minimize the effect of tissue motion is dependent on the beam profile of the transducer, the rate of tissue motion and the inhomogeneity of the underlying tissue. We further investigated the effect of the number of frames in the time series on tissue classification to determine the minimum number of required frames. We show that RF time series lengths as short as 64 frames may be sufficient for accurate tissue characterization. Obtaining a time series of 64 frames can be typically completed in less than two seconds using clinical settings on the ultrasound machine.

In *ex vivo* experiments, the main predicted zones of ablation generated from the selected RF time series features of a limited number of ROIs, and extended to the entire imaging planes closely resemble the gross pathology, but are not perfect matches in all cases for the following reasons: i) there is a misregistration between the ultrasound image and the gross pathology due to tissue deformation; ii) outlines of ablation are not necessarily visible in gross pathology; we have determined the ablation region based on the tissue color change rather than the microscopic pathology, iii) the number of selected ROIs for training may not be sufficient to perfectly extrapolate tissue differentiation to the entire tissue, and iv) there is no reliable ultrasound data from the shadows underneath the ablator, which would affect the classifier output for those regions.

It should be noted that the characterization capabilities of RF time series have been successfully demonstrated elsewhere with different users, transducers and systems, and extensive parameter ranges, for differentiation between various *ex vivo* animal tissue types and identification of prostate cancer in *ex vivo* human prostate [33], [37], [46]. We plan to extend this study to assess the effect of various ultrasound transducers.

Future work will focus on more extensive *in situ* experiments, predicting tissue ablation *in vivo*, and expanding the current method for ablation monitoring. In particular, large scale studies should be performed to determine the best combination of features for specific clinical applications. Moreover, we are investigating more accurate registration of the gross pathology to ultrasound images by using external fiducial landmarks. If the proposed method is to be used for ablation monitoring, we need to overcome the challenge of identifying a ground truth during the ablation process. In the current study, where we report the results of the feasibility experiments on *ex vivo* tissue samples, substantial consideration was made to avoid any macroscopic motion while tissue coagulation progressed. For *in vivo* experiments, to reduce the effect of tissue motion, several considerations include: substantially increasing ultrasound acquisition frame rate through imaging only a region of interest in the tissue, deformable registration for motion compensation, and focusing on ablation applications where breathing artefacts and other movements generate minimal motion.

ACKNOWLEDGMENT

The authors would like to acknowledge the help of Lance Frith and Bruce Komadina for preparing the mechanical components used in the *in situ* experiments, and assisting with the experiments. This work was supported in part by the Natural Sciences and Engineering Research Council of Canada (NSERC) and the Canadian Institutes of Health Research (CIHR). Research reported in this paper was also supported in part by the National Cancer Institute of the National Institutes of Health under grant numbers R44CA112852 and R44CA134169. The content is solely the responsibility of the authors and does not necessarily represent the official views of the National Institutes of Health.

REFERENCES

[1] C. Maleke, and E.E. Konofagou, "Harmonic motion imaging for focused ultrasound (HMIFU): a fully integrated technique for sonication and monitoring of thermal ablation in tissues," *Physics in Medicine and Biology*, vol. 53, no. 6, pp. 1773–93, 2008.

[2] Y. Lau, T.W.T. Leung, S.C.H. Yu, and S.K.W. Ho, "Percutaneous Local Ablative Therapy for Hepatocellular Carcinoma: A Review and Look Into the Future," *Annals of Surgery*, vol. 237, no. 2, pp. 171–179, 2003.

[3] T.S. Ravikumar, and R.N Kaleya, "Cyrotherapy for liver tumors," in *Liver and Biliary Tract Surgery*, 2000, pp. 1576–1606.

[4] R. Adam, P. Majno, D. Castaing, R. Giovenardi, and H. Bismuth, "Treatment of irresectable liver tumours by percutaneous cryosurgery," *British Journal of Surgery*, vol. 85, no. 11, pp. 1493–4, 1998.

[5] S.M. Lee, J.Y. Won, D.Y. Lee, K.-H. Lee, K.S. Lee, Y.H. Paik, and J.K Kim, "Percutaneous cryoablation of small hepatocellular carcinomas using a 17-gauge ultrathin probe," *Clinical Radiology*, vol. 66, no. 8, pp. 752–759, 2011.

[6] B.W. Dong, P. Liang, X.L. Yu, X.Q. Zeng, P.J. Wang, L. Su, X.D. Wang, H. Xin, and S. Li, "Sonographically guided microwave coagulation treatment of liver cancer: an experimental and clinical study," *American Journal of Roentgenology*, vol. 171, no. 2, pp. 449–54, 1998.

[7] R. Martin, C. Scoggins, and K. McMasters, "Safety and Efficacy of Microwave Ablation of Hepatic Tumors: A Prospective Review of a 5-Year Experience," *Annals of Surgical Oncology*, vol. 17, no. 1, pp. 171–178, 2010.

[8] P. Haigron, J.L. Dillenseger, L. Limin, and J.L. Coatrieux, "Image-Guided Therapy: Evolution and Breakthrough [A Look At]," *IEEE Engineering in Medicine and Biology Society*, vol. 29, no. 1, pp. 100–104, 2010.

[9] C.M. Pacella, G. Bizzarri, G. Francica, A. Bianchini, S. De Nuntis, S. Pacella, A. Crescenzi, S. Taccogna, G. Forlini, Z. Rossi, J. Osborn, and R. Stasi, "Percutaneous Laser Ablation in the Treatment of Hepatocellular Carcinoma with Small Tumors: Analysis of Factors Affecting the Achievement of Tumor Necrosis," *Journal of vascular and interventional radiology*, vol. 16, no. 11, pp. 1447–1457, 2005.

[10] A. Schindl, M. Schindl, H. Pernerstorfer-Schon, and L. Schindl, "Low intensity laser therapy: A review," *Journal of Investigative Medicine*, vol. 48, no. 5, pp. 312–326, 2000.

[11] F. Brunello, A. Veltri, P. Carucci1, E. Pagano, G. Ciccone, P. Moretto, P. Sacchetto, G. Gandini, and M. Rizzetto, "Radiofrequency ablation versus ethanol injection for early hepatocellular carcinoma: A randomized controlled trial," *Scandinavian Journal of Gastroenterology*, vol. 43, no. 6, pp. 727–735, 2008.

[12] K.T. Brown, and L.A. Brody, "Percutaneous methods for ablation of hepatic neoplasms," in *Liver and Biliary Tract Surgery*, 2000, pp. 1565–1576.

[13] J. Mclaughlan, I. Rivens, T. Leighton, and G.T. Haar, "A study of bubble activity generated in ex vivo tissue by HIFU," *Ultrasound in Medicine and Biology*, vol. 36, no. 8, pp. 1327–44, 2010.

[14] C.J. Diederich, R.J. Stafford, W.H. Nau, E.C. Burdette, R.E. Price, and J.D. Hazle, "Transurethral ultrasound applicators with directional heating patterns for prostate thermal therapy: in vivo evaluation using magnetic resonance thermometry," *Medical Physics*, vol. 31, no. 2, pp. 405–13, 2004.

[15] E.C. Burdette, D.C. Rucker, J.M. Croom, C. Clarke, P. Stolka, P. Prakash, T. Juang, C.J. Diederich, E.M. Boctor, and R.J. Webster, "The ACUSITT ultrasonic ablator: first steerable needle with an integrated interventional tool," in *SPIE Medical Imaging*, 2010, pp. 76290V1–V10.

[16] E. Boctor, M. deOliveira, M. Choti, R. Ghanem, R. Taylor, G. Hager, and G. Fichtinger, "US Monitoring of Tissue Ablation Via Deformation Model and Shape Priors," in *MICCAI*, 2006, pp. 405–412.

[17] B. Quesson, C. Laurent, G. Maclair, B.D. deSenneville, C. Mougenot, M. Ries, T. Carteret, A. Rullier, and C.T. Moonen, "Real-time volumetric MRI thermometry of focused ultrasound ablation in vivo: a feasibility study in pig liver and kidney," *NMR in Biomedicine*, vol. 24, no. 2, pp. 145–153, 2010.

[18] R. Chopra, J. Wachsmuth, M. Burtnyk, M.A. Haider, and M.J. Bronskill, "Analysis of factors important for transurethral ultrasound prostate heating using MR temperature feedback," *Physics in Medicine and Biology*, vol. 51, no. 4, pp. 827–44, 2006.

[19] S.V. Esser, M.V.D. Bosch , P.J.V. Diest, W.T.M. Mali, I. Rinkes, and R.V. Hillegersberg, "Minimally invasive ablative therapies for invasive breast carcinomas: An overview of current literature," *World Journal of Surgery*, vol. 31, no. 12, pp. 2284–2292, 2007.

[20] S. Siebers, M. Schwabe, U. Scheipers, C. Welp, J. Werner, and H. Ermert, "Evaluation of Ultrasonic Texture and Spectral Parameters for Coagulated Tissue Characterization," in *IEEE International Ultrasonics, Ferroelectrics, and Frequency Control*, 2004, pp. 1804–1807.

[21] R. Yang, K.K. Kopecky, F.J. Rescorla, C.A. Galliani, E.X. Wu, and J.L. Grosfeld, "Sonographic and computedtomography characteristics of liver ablation lesions induced by high-intensity focused ultrasound," *Investigative Radiology*, vol. 28, no. 9, pp. 796–801, 1993.

[22] B.J. ODalya, E. Morrisb, G.P. Gavinc, J.M. OByrnea, and G.B. McGuinness, "High-power low-frequency ultrasound: A review of tissue dissection and ablation in medicine and surgery," *Journal of Materials Processing Technology*, vol. 200, no. 1–3, pp. 38–58, 2008.

[23] X. Zheng, and S. Vaezy, "An acoustic backscatter-based method for localization of lesions induced by high-intensity focused ultrasound," *Ultrasound in Medicine and Biology*, vol. 36, no. 4, pp. 610–622, 2010.

[24] N.L. Bush, I. Rivens, G.R.T. Haar, and J.C. Bamber, "Acoustic properties of lesions generated with an ultrasound therapy system," *Ultrasound in Medicine and Biology*, vol. 19, no. 9, pp. 789–801, 1993.

[25] S. Zhang, M. Wan, H. Zhong, C. Xu, Z. Liao, H. Liu, and S. Wang, "Dynamic changes of integrated backscatter, attenuation coefficient and bubble activities during high-intensity focused ultrasound (HIFU) treatment," *Ultrasound in Medicine and Biology*, vol. 35, no. 11, pp. 1828–1844, 2009.

[26] B. Mehrabani, V. Tavakoli, M.D. Abolhassani, J. Alirezaie, and A. Ahmadian, "An efficient temperature estimation using optical-flow in ultrasound B-mode digital images," in *Engineering in Medicine and Biology Society, International Conference of the IEEE*, 2008, pp. 86–89.

[27] H. Zhong, M.X. Wan, Y.F. Jiang, and S.P. Wang, "Monitoring imaging of lesions induced by high intensity focused ultrasound based on differential ultrasonic attenuation and integrated backscatter estimation," *Ultrasound in Medicine and Biology*, vol. 33, no. 1, pp. 82–94, 2007.

[28] P.D. Bevan, and M.D. Sherar, "B-scan ultrasound imaging of thermal coagulation in bovine liver: log envelope slope attenuation mapping," *Ultrasound in Medicine and Biology*, vol. 27, no. 3, pp. 379–87, 2001.

[29] S. Siebers, U. Scheipers, M. Ashfaq, J. Hansler, M. Frieser, D. Strobel, E. Hahn, and H. Ermert, "In Vivo Imaging of Coagulated Tissue," in *IEEE Ultrasonics Symposium*, 2006, pp. 1762–1765.

[30] R.E. Kumon, Y. Zhou, K. Yang, and C.X. Deng, "Spectral Analysis of Ultrasound Backscatter for Characterization of HIFU Lesions in Cardiac Tissue with High-Frequency Imaging," in *IEEE International Ultrasonics Symposium Proceedings*, 2009, pp. 244–247.

[31] H. Rivaz, I. Fleming, L. Assumpcao, G. Fichtinger, U. Hamper, M. Choti, G. Hager, and E. Boctor, "Ablation Monitoring with Elastography: 2D In-vivo and 3D ex vivo Studies," in *MICCAI*, 2008, pp. 458–466.

[32] B.J. Fahey, K.R. Nightingale, D.L. Stutz, and G.E. Trahey, "Acoustic radiation force impulse imaging of thermally and chemically-induced lesions in soft tissues: preliminary ex vivo results," *Ultrasound in Medicine and Biology*, vol. 30, no. 3, pp. 321–8, 2004.

[33] M. Moradi, P. Abolmaesumi, and P. Mousavi, "Tissue typing using ultrasound RF time series: Experiments with animal tissue samples," *Medical Physics*, vol. 37, no. 8, pp. 4401–13, 2010.

[34] M. Aboofazeli, P. Abolmaesumi, M. Moradi, E. Sauerbrei, R. Siemens, A. Boag, and P. Mousavi, "Automated detection of prostate cancer using wavelet transform features of ultrasound RF time series," in *SPIE Medical Imaging*, 2009, pp. 72603J1–J8.

[35] F. Imani, P. Mousavi, M.I. Daoud, M. Moradi, and P. Abolmaesumi, "Tissue classification using depth-dependent ultrasound time series analysis: in-vitro animal study," in *SPIE Medical Imaging*, 2011, pp. 79680F1–79680F7.

[36] F. Imani, M. Wu, A. Lasso, E C. Burdette, M.I. Daoud, G. Fichtinger, P. Abolmaesumi, and P. Mousavi, "Monitoring of tissue ablation using time series of ultrasound RF data," in *MICCAI*, 2011, pp. 379–86.

[37] M. Moradi, P. Abolmaesumi, R. Siemens, E. E. Sauerbrei, A. H. Boag, and P. Mousavi, "Augmenting detection of prostate cancer in transrectal ultrasound images using SVM and RF time series," *IEEE Transactions on Biomedical Engineering*, vol. 56, no. 9, pp. 2214–24, 2009.

[38] E. Feleppa, A. Kalisz, J.B. Sokil-Melgar, F. Lizzi, T. Liu, A.L. Rosado, M.C. Shao, W.R. Fair, Y. Wang, M.S. Cookson, V.E. Reuter, and W. Heston, "Typing of prostate tissue by ultrasonic spectrum analysis," *IEEE Transactions on Ultrasonics Ferroelectrics and Frequency Control*, vol. 43, no. 4, pp. 609–619, 1996.

[39] C. A. Perez, and S. A. Sapareto, "Thermal dose expression in clinical hyperthermia and correlation with tumor response/control," *Cancer Research*, vol. 44, no. 10, pp. 4818s–25s, 1984.

[40] A. Accardo, M. Affinito, M. Carrozzi, and F. Bouquet, "Use of the fractal dimension for the analysis of electroencephalographic time series," *Biological Cybernetics*, vol. 77, no. 5, pp. 339–50, 1997.

[41] E.J. Feleppa, C.R. Porter, J. Ketterling, P. Lee, S. Dasgupta, S. Urban, and A. Kalisz, "Recent developments in tissue-type imaging (TTI) for planning and monitoring treatment of prostate cancer," *Ultrasonic Imaging*, vol. 26, no. 3, pp. 163–72, 2004.

[42] E.J. Feleppa, F.L. Lizzi, D.J. Coleman, and M.M. Yaremko, "Diagnostic spectrum analysis in ophthalmology: a physical perspective," *Ultrasound in Medicine and Biology*, vol. 12, no. 8, pp. 623–31, 1986.

[43] S. Siebers, M. Schwabe, U. Scheipers, C. Welp, J. Werner, and H. Ermert, "Evaluation of ultrasonic texture and spectral parameters for coagulated tissue characterization," in *IEEE Ultrasonics Symposium*, 2004, pp. 1804–1807.

[44] S. Siebers, U. Scheipers, J. Hnsler, M. Frieser, D. Strobel, C. Welp, J. Werner, E. Hahn, and H. Ermert, "Classification of thermally ablated tissue using diagnostic ultrasound," *Acoustical Imaging*, vol. 28, pp. 295–300, 2007.

[45] C. Leung, K. Hashtrudi-Zaad, P. Foroughi, and P. Abolmaesumi, "A real-time intra-subject elastic registration algorithm for dynamic 2D ultrasound images," *Ultrasound in Medicine and Biology*, vol. 35, no. 7, pp. 1159–76, 2009.

[46] M. I. Daoud, P. Mousavi, F. Imani, R. Rohling, and P. Abolmaesumi, "Computer-aided tissue characterization using ultrasound-induced thermal effects: analytical formulation and in-vitro animal study," in *SPIE Medical Imaging*, 2011, pp. 79680G1–79680G6.